International Journal of Scientific World, *12 (1) (2026) 32-47*

International Journal of Scientific World

Website: www.sciencepubco.com/index.php/IJSW
https://doi.org/10.14419/zfk3hm26
Research paper

Computational Investigation of Magneto-Hydro-Dynamically Influenced Elastico-Viscous Williamson Nanofluid Flow Over A Nonlinear Stretching Interface

Bikash Koli Saha *

Independent Researcher, Mathematics, Guwahati, Kamrup Metropolitan, Assam, PIN:781018, India
**Corresponding author E-mail: bikashkoli100@gmail.com*

Received: 18-07-2026, Accepted: 18-07-2026, Published: 10-08-2026

Abstract

A rigorous computational analysis is conducted to examine the influence of magnetohydrodynamic effects on the flow of an elastico-viscous Williamson nanofluid over a nonlinearly stretching surface within a suitably defined geometrical framework. The governing partial differential equations describing the fluid motion are systematically transformed into a system of coupled, highly nonlinear ordinary differential equations through the implementation of appropriate similarity transformations, along with the imposition of relevant boundary conditions. These resulting nonlinear equations are numerically solved using the MATLAB built-in boundary value solver bvp4c, incorporating the transformed boundary constraints to extract detailed physical interpretations of the governing flow parameters. The behavior of velocity, temperature, and concentration distributions is thoroughly analyzed, revealing that the velocity field exhibits pronounced fluctuations and oscillatory characteristics in the vicinity of the stretching surface. In contrast, both the thermal and concentration profiles demonstrate a monotonic decay for most variations of the controlling parameters. Furthermore, the study highlights that the inclusion of the elastico-viscous parameter significantly alters the overall flow dynamics within the boundary layer region.

Keywords: *Magneto-Hydrodynamic; Elastico-Viscous; Similarity Transformation; Non-Linear Stretching Sheet; Williamson Nanofluid.*

1. Introduction

Fluid mechanics is broadly classified into Newtonian and non-Newtonian regimes. For fluids that deviate from the classical Newtonian viscosity law, the strain rate–stress relationship is characterized through constitutive formulations. To capture the complex rheological behavior of such materials, numerous theoretical models have been developed by researchers. Williamson [1] introduced a constitutive framework for pseudoplastic substances that has been substantiated through experimental validation. A distinctive feature of this formulation is the simultaneous incorporation of both the lower (μ_0) and upper (μ_∞) bounds of viscosity. For realistic fluid representation, accounting for these limiting viscosities is essential within the mathematical structure. Such pseudo-plastic media find widespread industrial relevance, particularly in processes involving high–molecular-weight polymeric melts, the fabrication processes of photographic films, and the extrusion of polymeric sheet structures, operations studied by Felder and Levrau [2]. Nadeem and Akbar [3] numerically investigated the peristaltically induced transport mechanism of a Williamson fluid within an endoscopic configuration, incorporating radially varying magnetohydrodynamic effects to elucidate complex flow behavior. Berra et al. [4] examined how incorporating nanosilica modifies the workability and enhances the mechanical strength behavior of Portland cement paste under compressive loading conditions.

Investigating the rheological behavior of dilute magnetic Fe_3O_4 nanoparticle suspensions in ethylene glycol–water mixtures, this study elucidates the viscosity characteristics under low particle concentration regimes by Sundar et al. [5]. Azmi et al. [6] conducted an experimental analysis of turbulent forced convection, demonstrating that the incorporation of SiO_2 nanofluid significantly augments heat transfer efficiency while simultaneously modifying the associated frictional resistance. In the context of non-Newtonian transport phenomena, Nadeem et al. [7-8] explored the boundary-layer flow of a Williamson fluid over a stretching surface, providing critical understanding of the rheological parameters governing momentum transport. Furthermore, Akbar and Nadeem [9] developed a theoretical model based on the Carreau fluid formulation to investigate blood flow dynamics, elucidating the impacts of arterial tapering and stenosis on hemodynamic behavior.

Azmi et al. [10] conducted a rigorous comparative analysis on the augmentation of convective heat transfer and the associated hydrodynamic resistance of TiO_2-based nanofluid flow within a tubular configuration fitted with twisted tape inserts, thereby revealing the coupled influence of nanoparticle-induced thermal conductivity enhancement and swirl-induced flow intensification mechanisms. Sreedevi et al. [11] performed a comprehensive assessment of the simultaneous heat and mass transfer processes in nanofluid flow over both linearly and nonlinearly stretching surfaces, explicitly accounting for the critical contributions of thermal radiation and chemically reactive species on

Copyright © Bikash Koli Saha. This is an open access article distributed under the Creative Commons Attribution License, which permits unrestricted use, distribution, and reproduction in any medium, provided the original work is properly cited.

transport characteristics. Furthermore, Jahan et al. [12] advanced the theoretical framework by investigating nanofluid flow over a permeable nonlinear stretching/shrinking surface through an improved modeling approach, complemented by a stability analysis to ensure the physical admissibility and robustness of the obtained solutions.

Khan et al. [13] significantly refine the theoretical modeling of heat transfer by integrating the Cattaneo–Christov heat flux formulation with the Optimal Homotopy Analysis Method (OHAM), thereby facilitating a rigorous comparative evaluation of the transient responses exhibited by three different nanofluid configurations. Hussain et al. [14] examine the magnetohydrodynamic convective transport characteristics of a Williamson fluid in the presence of coupled homogeneous and heterogeneous chemical reactions, presenting a detailed comparative assessment between flow regimes over a stretching sheet and a cylindrical geometry. Ahmed et al. [15] develop an effective similarity transformation approach that systematically reduces the governing equations, enabling precise analysis of MHD Williamson nanofluid flow induced by a nonlinearly stretching surface. Muzara and Shateyi [16] propose a comprehensive investigation into the coupled effects of magnetic field intensity, chemical reaction mechanisms, and thermal radiation on Williamson nanofluid flow over an exponentially stretching sheet. Rashad et al. [17] explore the thermal transport phenomena of MHD Williamson hybrid nanofluids within porous media, with particular emphasis on the roles of convective boundary conditions and Joule (Ohmic) heating effects.

The investigation conducted by Khan et al. [18] rigorously examines the coupled thermal and solutal transport phenomena in magnetohydrodynamic Williamson nanofluid flow over a stretching surface, thereby elucidating significant aspects of its temperature and concentration distributions. Kumar et al. [19] present an advanced analysis on the role of cross-diffusion mechanisms in MHD Williamson nanofluid flow across a nonlinear stretching sheet embedded in a permeable medium, offering deeper insight into multi-transport interactions. Furthermore, Sakkaravarthi and Bala [20] explore the irreversibility characteristics through entropy generation in MHD Williamson hybrid nanofluid flow over a permeable curved stretching/shrinking surface, emphasizing the impact of diverse radiative effects on both thermal transport and flow dynamics.

Ramadevu et al. [21] conduct a comprehensive numerical analysis to elucidate the coupled mechanisms of heat and mass transport in magnetohydrodynamic Williamson nanofluid flow induced by a nonlinearly stretching surface, while rigorously incorporating the influences of viscous dissipation and thermal radiation. Gizachew et al. [22] examine the transient characteristics of Williamson nanofluid subjected to time-dependent MHD flow over a thermally energized, permeable, and inclined stretching sheet situated within a porous medium. Sankari et al. [23] provide an analytical framework to investigate MHD-driven bio-convective transport in Williamson nanofluid flow over an exponentially stretching surface, explicitly accounting for viscous dissipation effects alongside the dynamics of gyrotactic microorganisms.

This work examines the dynamics of magnetohydrodynamic flow of a Williamson nanofluid over a nonlinearly stretching surface, accounting for the influence of elastico-viscous fluid characteristics. The analysis prioritizes the cumulative influence of the elastico-viscous Williamson parameter, rather than its spatial variability within the flow domain. A comprehensive parametric study is conducted to evaluate the roles of the magnetic interaction parameter, Prandtl number, diffusivity ratio, elastico-viscous parameter, Williamson parameter, Schmidt number, Lewis number, and heat capacity ratio on the velocity, thermal, and concentration fields, with results systematically presented through graphical representations.

2. Mathematical Formulation

A steady, planar MHD boundary-layer formulation is developed for an incompressible Williamson nanofluid over a nonlinearly stretching sheet, accounting for elastico-viscous behavior. The surface extends along the xxx-direction with stretching velocity. $u = U_w = Bx^{\frac{1}{3}}$, while y is taken normal to the sheet. A non-uniform transverse magnetic field $B* = \frac{B_0}{x^{\frac{1}{3}}}$ is imposed perpendicular to the flow. The boundary conditions prescribe U_w, T_w, and C_w at the wall for velocity, temperature, and concentration, respectively, whereas the far-field state is defined by T_∞ and C_∞.

The fundamental equations governing conservation of mass, momentum, thermal energy, and species concentration are formulated as follows:

$$\frac{\partial u}{\partial x} + \frac{\partial v}{\partial y} = 0 \tag{2.1}$$

$$u\frac{\partial u}{\partial x} + v\frac{\partial u}{\partial y} = \upsilon\,\frac{\partial^2 u}{\partial y^2} + \sqrt{2}\,\Gamma\,\upsilon\,\frac{\partial u}{\partial y}\frac{\partial^2 u}{\partial y^2} - \sigma\frac{B*^2}{\rho}u - \frac{k_0}{\rho}\left[u\frac{\partial^3 u}{\partial x\,\partial y^2} + v\frac{\partial^3 u}{\partial y^3} - \frac{\partial u}{\partial y}\frac{\partial^2 u}{\partial x\,\partial y} - \frac{\partial v}{\partial y}\frac{\partial^2 u}{\partial y^2}\right] = 0 \tag{2.2}$$

$$u\frac{\partial T}{\partial x} + v\frac{\partial T}{\partial y} = \alpha\frac{\partial^2 T}{\partial y^2} + \frac{\rho_p\,c_p}{\rho C}\left[D_B\,\frac{\partial T}{\partial y}\,\frac{\partial C}{\partial y} + \left(\frac{D_T}{T_\infty}\right)\left(\frac{\partial T}{\partial y}\right)^2\right] \tag{2.3}$$

$$u\frac{\partial C}{\partial x} + v\frac{\partial C}{\partial y} = D_B\frac{\partial^2 C}{\partial y^2} + \left(\frac{D_T}{T_\infty}\right)\frac{\partial^2 T}{\partial y^2} \tag{2.4}$$

Illustration of MHD-driven elastico-viscous Williamson nanofluid over a nonlinear stretching sheet, highlighting the interplay of Lorentz force, Brownian diffusion, elastico-viscous shear-thinning behavior, nanoparticle thermophoresis, and thermal radiation, producing coupled velocity, thermal, and concentration distributions in Fig. 2.1.

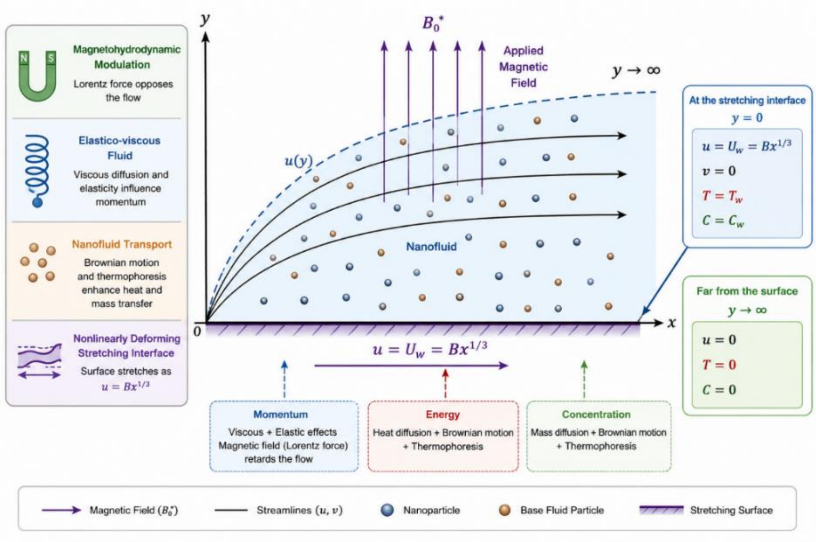

Fig. 2.1: Physical Flow Problem.

The associated boundary constraints are prescribed in the following form.

$$u = U_w = Bx^{\frac{1}{3}}, v = 0, T = T_w, C = C_w \text{ at } y = 0 \tag{2.5}$$

$$u = 0, T = 0, C = 0 \text{ as } y \to \infty \tag{2.6}$$

The ensuing analysis employs the following similarity transformations to reduce the governing equations into a dimensionless form:

$$\zeta = x^{-\frac{1}{3}}\sqrt{\frac{B}{\upsilon}}\, y, u = Bx^{\frac{1}{3}} f'(\zeta), v = -\frac{\sqrt{\upsilon B}}{3\, x^{\frac{1}{3}}}[\, 2\, f(\zeta) - \zeta f'(\zeta)], \theta(\zeta) = \frac{T - T_\infty}{T_w - T_\infty}, \phi(\zeta) = \frac{C - C_\infty}{C_w - C_\infty} \tag{2.7}$$

Substituting equation (2.7) into equations (2.1) – (2.6) yields the resulting system of governing equations:

$$3f'''(\zeta) + 2f(\zeta)f''(\zeta) + \lambda f''(\zeta)f'''(\zeta) - Mf' - f'^2 + 2k_1 f(\zeta)f^{iv}(\zeta) = 0 \tag{2.8}$$

$$\theta''(\zeta) + \frac{2}{3}\Pr f(\zeta)\theta'(\zeta) + \frac{Nc}{Le}\,\phi'(\zeta)\theta'(\zeta) + \frac{Nc}{Le.Nbt}\,\theta'^2 = 0 \tag{2.9}$$

$$\phi''(\zeta) + \frac{2}{3}Sc\, f(\zeta)\phi'(\zeta) + \frac{1}{Nbt}\,\theta''(\zeta) = 0 \tag{2.10}$$

$$f = 0, f' = 1, \theta = 1, \phi = 1, \phi' = 0, \text{at } \zeta \to 0 \tag{2.11}$$

$$f' = 0, \theta = 0, \phi = 1 \text{ at } \zeta \to \infty \tag{2.12}$$

The dimensionless parameters are defined as follows: the Williamson parameter. $\lambda = 3\Gamma\sqrt{\frac{2B^3}{\upsilon}}$, the magnetic parameter $M = \frac{3\sigma B_0^2}{B\rho}$, and the elastic parameter $k_1 = \frac{k_0 B}{\rho\upsilon x^{\frac{2}{3}}}$, . The Prandtl number is given by $Pr = \frac{\upsilon}{\alpha}$, while the heat capacity ratio is $Nc = \frac{\rho_p C_p}{\rho c}(C_w - C_\infty)$. In addition, the Lewis number is $Le = \frac{\upsilon}{D_B}$, and the diffusivity parameter is expressed as $Nbt = \frac{D_B T_\infty (C_w - C_\infty)}{D_T (T_w - T_\infty)}$.
By setting $\lambda = M = k_1 = 0$ in equations (2.8), the governing framework asymptotically degenerates into the classical viscous boundary layer formulation, indicating that the fluid exhibits purely Newtonian behavior.

3. Method of Solution

The nonlinear similarity mappings (2.8) – (2.12) are recast into an equivalent canonical framework comprising a coupled system of first-order ordinary differential equations:

$$f = \delta_1, f' = \delta_2, f'' = \delta_3, f''' = \delta_4, \theta = \delta_5, \theta' = \delta_6, \phi = \delta_7, \phi' = \delta_8 \tag{3.1}$$

Equation (3.1) facilitates the systematic formulation of

$$\delta_1' = \delta, \delta_2' = \delta_3, \delta_3' = \delta_4, \delta_5' = \delta_6, \delta_7' = \delta_8 \tag{3.2}$$

By applying the similarity transformations given in (3.1) and (3.2), the governing equations (2.8) – (2.10) are transformed into the following reduced system of equations:

$$\delta_4' = \frac{-1}{2k_{1\delta_1}}(3\delta_4 + 2\delta_1\delta_3 + \lambda\delta_3\delta_4 - M\delta_2 - \delta_2^2) \tag{3.3}$$

$$\delta_6' = -\left(\frac{2}{3}\,\mathrm{Pr}\delta_1\delta_6 + \frac{\mathrm{Nc}}{\mathrm{Le}}\delta_6\delta_8 + \frac{\mathrm{Nc}}{\mathrm{Le.Nbt}}\,\delta_6^2\right) \tag{3.4}$$

$$\delta_8' = -\left(\frac{2}{3}\,\mathrm{Sc}\delta_1\delta_8 + \frac{1}{\mathrm{Nbt}}\,\delta_6'\right) \tag{3.5}$$

The transformed boundary conditions given in equations (2.11) and (2.12) can be concisely rewritten in their reduced form as follows:

$$\delta_1(0) = 0,\ \delta_2(0) = 1,\ \delta_5(0) = 1,\ \delta_7(0) = 1,\ \delta_8(0) = 0 \tag{3.6}$$

$$\delta_2(\infty) = 0,\ \delta_5(\infty) = 0,\ \delta_7(\infty) = 0 \tag{3.7}$$

The coupled boundary-layer equations (3.3) – (3.5), together with the boundary conditions (3.6) – (3.7), are solved numerically using the MATLAB bvp4c solver, ensuring reliable and precise solutions across a wide spectrum of governing flow parameters.

4. Numerical Analysis

The dimensionless skin-friction coefficient, temperature gradient, and concentration gradient are computed numerically by considering the elastico-viscous parameter (k_1) = 0.

Table 1: Influence of Governing Physical Parameters on the Dimensionless Skin-Friction Coefficient $-F''(0)$

λ	M	Pr	Nbt	Nc	Le	Sc	$-f''(0)$
0.1	0.5	0.5	2.0	0.5	3.0	2.0	0.7954
0.2	0.5	0.5	2.0	0.5	3.0	2.0	0.8024
0.3	0.5	0.5	2.0	0.5	3.0	2.0	0.8097
0.5	0.1	0.5	2.0	0.5	3.0	2.0	0.7296
0.5	0.2	0.5	2.0	0.5	3.0	2.0	0.7544
0.5	0.3	0.5	2.0	0.5	3.0	2.0	0.7786

Table 2: Influence of Governing Physical Parameters on Dimensionless Temperature Gradient $-\Theta'(0)$

λ	M	Pr	Nbt	Nc	Le	Sc	$-\theta'(0)$
0.1	0.5	0.5	2.0	0.5	3.0	2.0	0.2607
0.2	0.5	0.5	2.0	0.5	3.0	2.0	0.2603
0.3	0.5	0.5	2.0	0.5	3.0	2.0	0.2598
0.5	0.1	0.5	2.0	0.5	3.0	2.0	0.2681
0.5	0.2	0.5	2.0	0.5	3.0	2.0	0.2656
0.5	0.3	0.5	2.0	0.5	3.0	2.0	0.2633
0.5	0.5	0.1	2.0	0.5	3.0	2.0	0.1434
0.5	0.5	0.2	2.0	0.5	3.0	2.0	0.1703
0.5	0.5	0.3	2.0	0.5	3.0	2.0	0.1989
0.5	0.5	0.5	0.4	0.5	3.0	2.0	0.2260
0.5	0.5	0.5	0.5	0.5	3.0	2.0	0.2336
0.5	0.5	0.5	0.6	0.5	3.0	2.0	0.2389
0.5	0.5	0.5	2.0	0.1	3.0	2.0	0.2941
0.5	0.5	0.5	2.0	0.2	3.0	2.0	0.2849
0.5	0.5	0.5	2.0	0.3	3.0	2.0	0.2759
0.5	0.5	0.5	2.0	0.5	0.3	2.0	0.0570
0.5	0.5	0.5	2.0	0.5	0.4	2.0	0.0878
0.5	0.5	0.5	2.0	0.5	0.5	2.0	0.1134
0.5	0.5	0.5	2.0	0.5	3.0	0.1	0.2776
0.5	0.5	0.5	2.0	0.5	3.0	0.2	0.2759
0.5	0.5	0.5	2.0	0.5	3.0	0.3	0.2741

Table 3: Influence of Governing Physical Parameters on Dimensionless Concentration Gradient $-\Phi'(0)$

λ	M	Pr	Nbt	Nc	Le	Sc	$-\phi'(0)$
0.1	0.5	0.5	2.0	0.5	3.0	2.0	0.6788
0.2	0.5	0.5	2.0	0.5	3.0	2.0	0.6778
0.3	0.5	0.5	2.0	0.5	3.0	2.0	0.6767
0.5	0.1	0.5	2.0	0.5	3.0	2.0	0.6926
0.5	0.2	0.5	2.0	0.5	3.0	2.0	0.6879
0.5	0.3	0.5	2.0	0.5	3.0	2.0	0.6833
0.5	0.5	0.1	2.0	0.5	3.0	2.0	0.7281
0.5	0.5	0.2	2.0	0.5	3.0	2.0	0.7143
0.5	0.5	0.3	2.0	0.5	3.0	2.0	0.7007
0.5	0.5	0.5	0.4	0.5	3.0	2.0	0.4726
0.5	0.5	0.5	0.5	0.5	3.0	2.0	0.5175
0.5	0.5	0.5	0.6	0.5	3.0	2.0	0.5494
0.5	0.5	0.5	2.0	0.1	3.0	2.0	0.6656
0.5	0.5	0.5	2.0	0.2	3.0	2.0	0.6679
0.5	0.5	0.5	2.0	0.3	3.0	2.0	0.6702
0.5	0.5	0.5	2.0	0.5	0.3	2.0	0.7243
0.5	0.5	0.5	2.0	0.5	0.4	2.0	0.7166
0.5	0.5	0.5	2.0	0.5	0.5	2.0	0.7104
0.5	0.5	0.5	2.0	0.5	3.0	0.1	0.0983
0.5	0.5	0.5	2.0	0.5	3.0	0.2	0.1285
0.5	0.5	0.5	2.0	0.5	3.0	0.3	0.1606

Table 4: The Value of $-\Theta'(0)$ by Considering Fixed Values of $\Lambda = 0.2$, $M = 0$, $Pr = 0.5$, $Nbt = 2$, $Nc = 0.5$, $Le = 4$, and $Sc = 0.5$

λ	Pr	Nadeem et al. [8]	Ahmed et al.[16]	Present Study
0.0		0.314	0.319	0.294
0.2		0.309	0.318	0.293
0.4		0.302	0.317	0.292
	0.2	0.144	0.231	0.189
	0.6	0.355	0.347	0.328
	1.2	0.588	0.521	0.522

5. Results and Discussion

The velocity, temperature, and concentration are studied in this research. The solutions and their impact are discussed by considering fixed fluid flow parameters along with the various elastico-viscous parameters. The fixed parameters and their variation are indicated in the corresponding figures.

Velocity Profile: The dimensionless velocity $f'(\zeta)$ against ζ are plotted in Figs. 4.1−4.8. The velocity distribution oscillates at $f'(\zeta) = 1$ when $\zeta = 8$ in all cases and finally settled down at $f'(\zeta) = 0$ when $\zeta = 8$. The fluid velocity shows this kind of pattern due to the influence of elastico-viscous fluid in combination with water-based nanofluid. The fluid velocity slightly declines during its oscillation pattern from initial flow to the final flow at the non-linear surface.

From Fig: 4.1: The velocity distribution $f'(\zeta)$ against ζ exhibits pronounced oscillatory behavior with increasing elastico-viscous parameter k_1(0.7–0.9). Concurrently, an appreciable thickening of the momentum boundary layer is observed as k_1 intensifies. This non-monotonic response originates from the intricate interplay among Lorentz forces, elastico-viscous resistance, and nonlinear surface stretching, which collectively generate successive phases of acceleration and deceleration within the boundary layer regime.

From fig. 4.2: The velocity distribution $f'(\zeta)$ against ζ exhibits a pronounced oscillatory structure due to the interplay between magnetic damping, viscous resistance, and nonlinear stretching effects. An increase in the Williamson parameter λ ($0.1 \rightarrow 0.5$) significantly enhances the momentum transport within the boundary layer, leading to amplified velocity magnitudes. Consequently, both the peak enhancement and deeper trough formation are observed, indicating stronger inertial dominance over dissipative forces. This behavior reflects the intensified competition between flow acceleration and resistive mechanisms in the elastico-viscous nanofluid regime.

From Fig: 4.3: This graph shows the velocity profile $f'(\zeta)$ against ζ for varying magnitudes of the magnetic parameter M, an increment from ($0 \rightarrow 2$), yields a marginal amplification of velocity in the vicinity of the peak region, followed by a pronounced attenuation downstream. This behavior is attributed to the intensification of the Lorentz force induced by the applied magnetic field, which imposes an opposing resistive drag on the fluid motion. Consequently, elevated M enhances momentum suppression, leading to an overall deceleration of the flow field, particularly in regions removed from the peak velocity.

From Fig: 4.4: This plot shows how $f'(\zeta)$ against ζ for a spectrum of Prandtl number Pr magnitudes. As Pr increases ($1 \rightarrow 2$), the peak of $f'(\zeta)$ gets higher. This happens because higher Pr means lower thermal diffusivity, so momentum effects dominate, increasing the magnitude of the flow. The shape stays similar, but amplitude grows with Pr.

From Fig: 4.5: As Lewis number Le increases ($0.10 \rightarrow 0.20$), the velocity $f'(\zeta)$ against ζ decreases. This is because a higher Lewis number Le means lower mass diffusivity, which weakens concentration effects. Results in a smoother curve with smaller peaks.

From Fig: 4.6: As the diffusivity parameter Nbt increases ($0.4 \rightarrow 1.8$), the curve shifts downward, and the amplitude reduces. Higher Nbt increases nanoparticle diffusion, which smooths and weakens the fluid velocity. Hence, lower peaks and more damping in the flow.

From Fig: 4.7: The graph shows velocity $f'(\zeta)$ against ζ for different Nc values. Near the surface ($\zeta = 0$), velocity is high due to the stretching effect. As Nc increases, velocity decreases due to viscous resistance. Increasing Nc ($0 \rightarrow 4$), reduces peak velocity. Makes the boundary layer thinner and causes earlier decay of flow. An increase in Nc leads to stronger resistance, which results in a reduction in velocity and a more rapid decay of the flow.

From fig. 4.8: The graph shows velocity $f'(\zeta)$ against ζ for different Sc. Near the surface, velocity starts positive, then decreases sharply due to fluid resistance. As Sc increases, velocity recovers and approaches zero far from the surface. Increasing Sc ($1 \rightarrow 3$) provide enhances momentum resistance and reduces velocity magnitude, also making the boundary layer thinner. An increase in Sc leads to greater resistance, resulting in lower velocity and a more rapid decay of the flow.

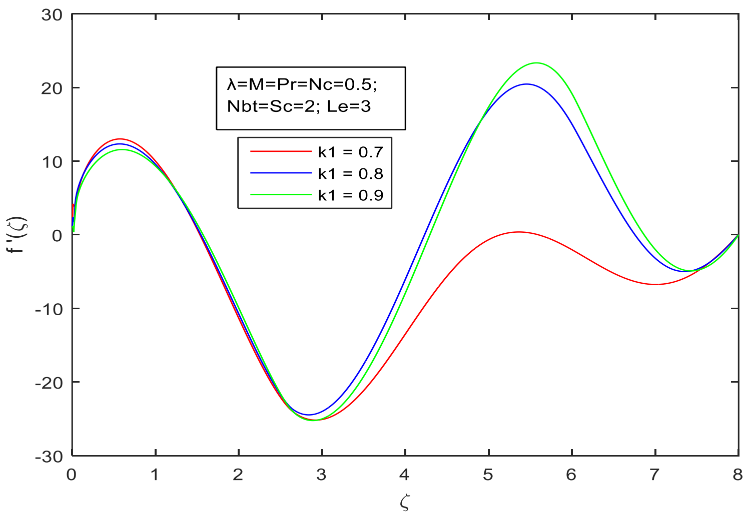

Fig. 4.1: Velocity with k_1.

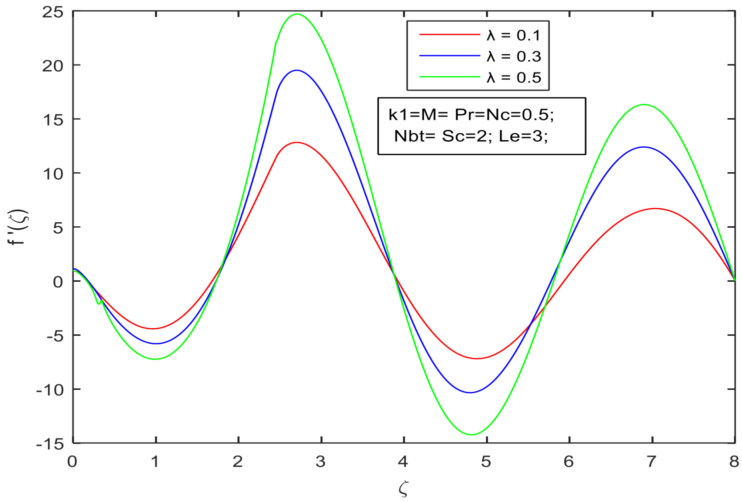

Fig. 4.2: Velocity with λ.

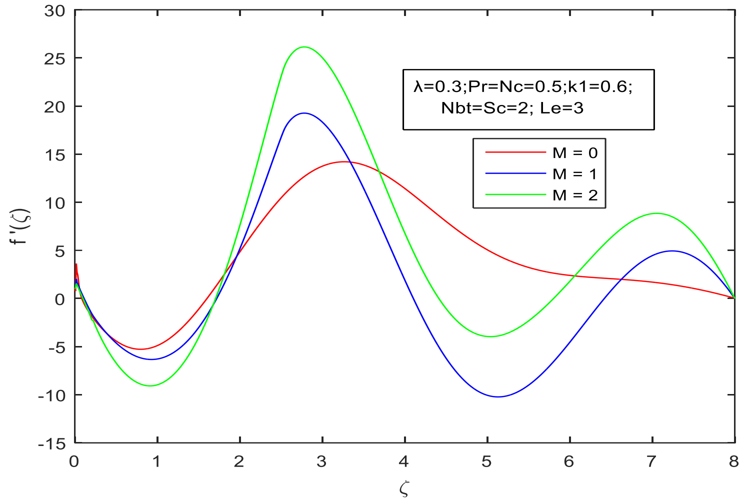

Fig. 4.3: Velocity with M.

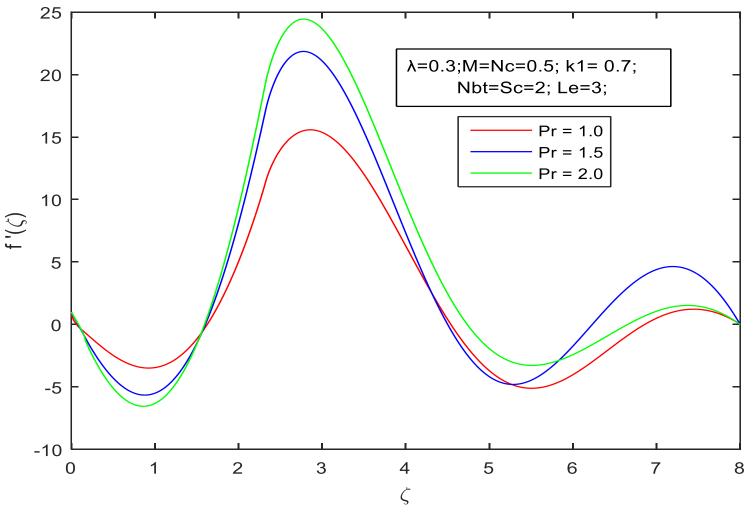

Fig. 4.4: Velocity with Pr.

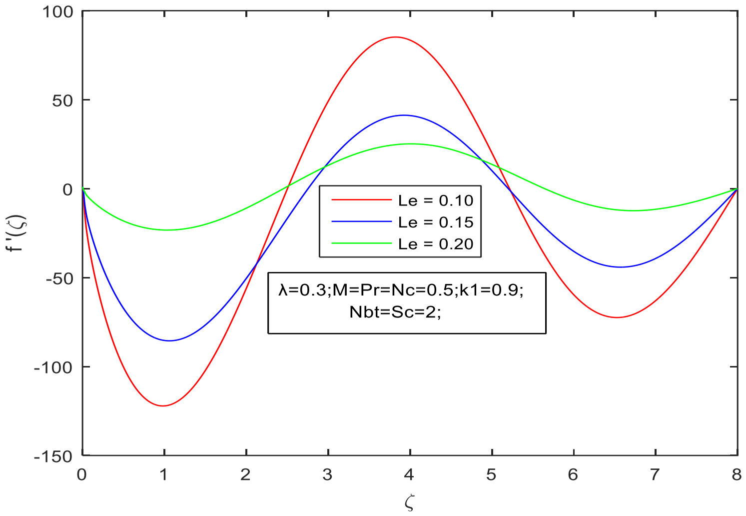

Fig. 4.5: Velocity with Le.

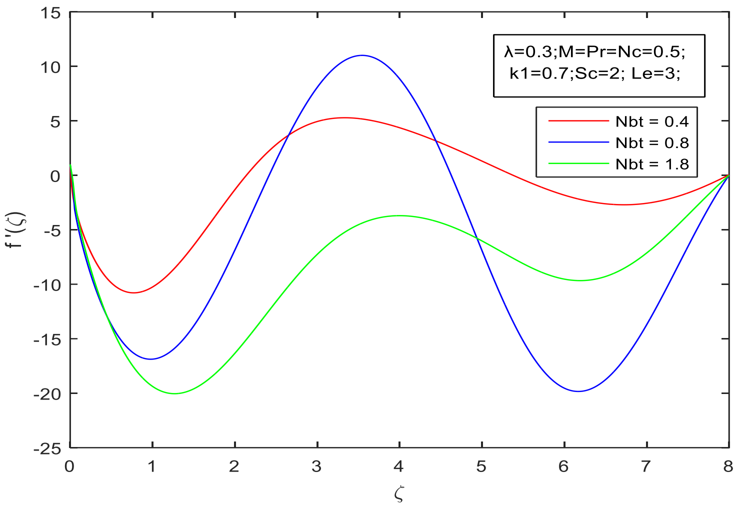

Fig. 4.6: Velocity with Nbt.

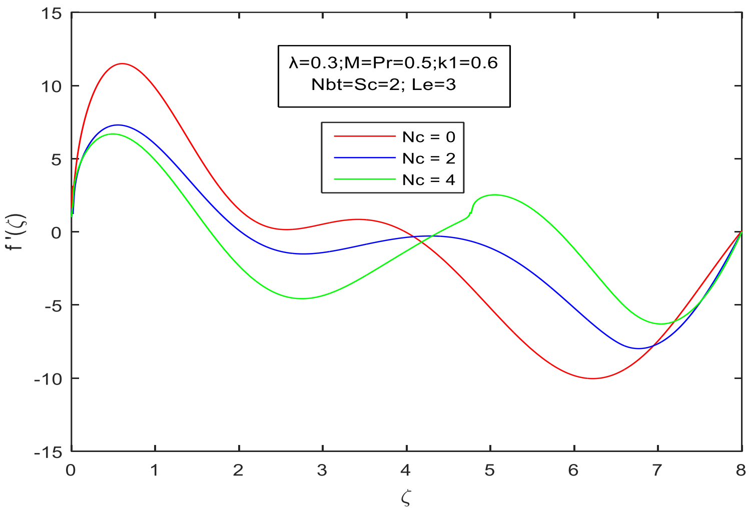

Fig. 4.7: Velocity with Nc.

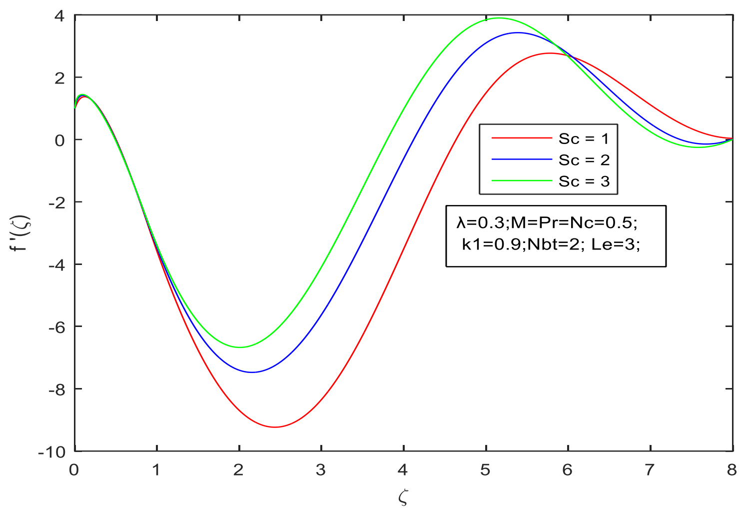

Fig. 4.8: Velocity with Sc.

Temperature Profile: The temperature $\theta(\zeta)$ against ζ are plotted in Figs. 4.9−4.16. The temperature of the fluid decreases for all the fluid flow parameters involved in the flow field. The temperature flows from $\theta(\zeta) = 1$ at $\zeta = 0$ to $\theta(\zeta) = 0$ at $\zeta = 8$ at the stretching sheet.

From Fig: 4.9: The graph shows temperature $\theta(\zeta)$ against ζ for different k_1 values. Temperature starts high at the surface and decreases with ζ due to heat diffusion. Increasing k_1 $(0.7 \rightarrow 0.9)$ reduces the heat loss effect and raises the temperature distribution, also making the thermal boundary layer thicker. Augmentation of k_1 intensifies the thermal field, yielding elevated temperature levels accompanied by a more gradual attenuation of the thermal boundary layer.

From Fig: 4.10: The graph shows temperature $\theta(\zeta)$ against ζ for varying values of the Williamson parameter λ, the thermal field exhibits a monotonic decay from the wall to the ambient state. An escalation in λ $(0.1 \rightarrow 0.3)$ intensifies the fluid's thermal energy, thereby augmenting the temperature magnitude throughout the boundary layer. This elevation in temperature distribution signifies a pronounced thickening of the thermal boundary layer, accompanied by a retarded attenuation of the thermal profile.

From Fig. 4.11: This plot shows how temperature $\theta(\zeta)$ decreases along a surface for varying magnitudes of the magnetic interaction parameter M. The temperature curves $\theta(\zeta)$ against ζ, indicating that the temperature cools along the distance. A higher value of M $(0 \rightarrow 2)$ results in slower cooling, so the temperature remains higher for longer, while a lower value of M leads to faster cooling, causing the temperature to drop more quickly and even slightly undershoot. The curve represents a decaying temperature profile caused by heat transfer through conduction and convection, where the parameter. M controls resistance to heat flow, such that a larger M keeps the temperature higher for a longer distance.

From Fig: 4.12: This plot shows how temperature $\theta(\zeta)$ decreases along a surface for varying values of the Prandtl parameter; an elevation in Pr $(1 \rightarrow 2)$ signifies diminished thermal diffusivity, which contracts the thermal boundary layer thickness and accelerates the attenuation of the temperature profile.

From Fig: 4.13: The graph shows temperature $\theta(\zeta)$ against ζ for different values of Le. A higher Lewis number Le $(0.10 \rightarrow 0.20)$ attenuation of mass diffusivity suppresses species transport, thereby augmenting the thermal boundary layer thickness and sustaining elevated temperature profiles with a more gradual decay rate.

From Fig: 4.14: The temperature $\theta(\zeta)$ against ζ for different values of the diffusivity parameter Nbt. A higher diffusivity parameter Nbt $(0.4 \rightarrow 1.8)$ enhances nanoparticle diffusion, increasing thermal energy, so the temperature rises and decays more slowly.

From Fig: 4.15: The temperature $\theta(\zeta)$ against ζ for different values of heat capacity ratio parameter Nc. A higher heat capacity ratio Nc $(1 \rightarrow 3)$ increases the fluid's energy absorption capacity, resulting in a reduced temperature rise, a lower peak temperature, and a faster decay.

From Fig: 4.16: The variation of temperature $\theta(\zeta)$ against ζ under varying Schmidt number Sc reveals that an escalation in Sc $(1 \rightarrow 3)$ suppresses thermal diffusivity relative to mass diffusivity, thereby attenuating the temperature field and accelerating its spatial decay. This behavior is attributed to the reduced efficacy of thermal energy transport at higher. Sc, which contracts the thermal boundary layer thickness and induces a steeper temperature gradient away from the surface.

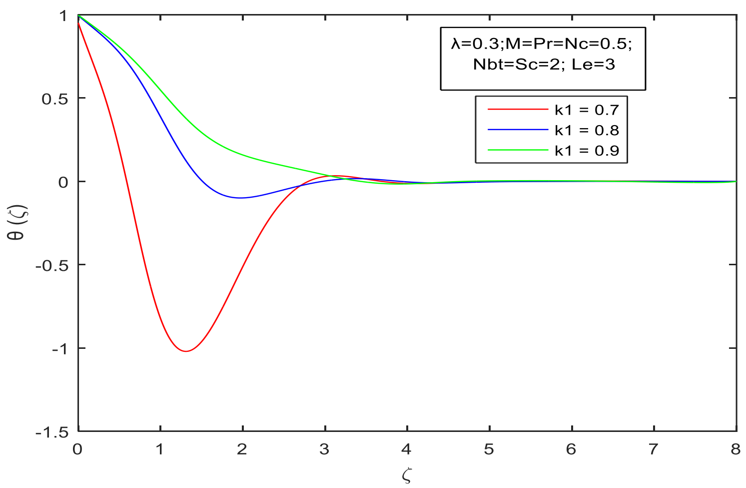

Fig. 4.9: Temperature with K1.

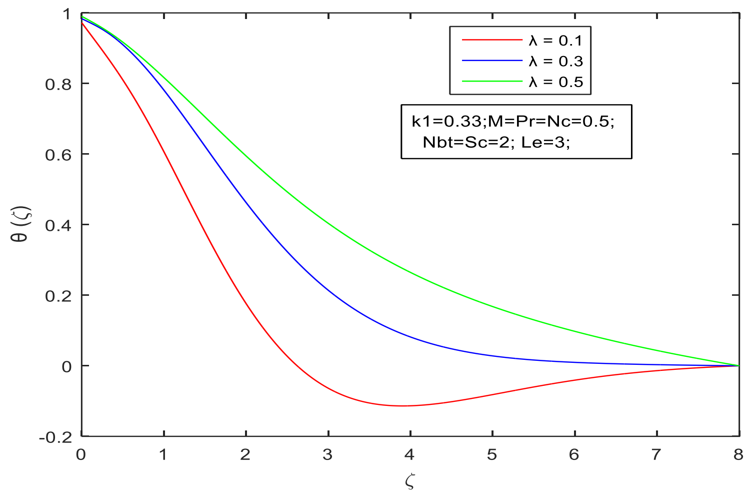

Fig. 4.10: Temperature with λ.

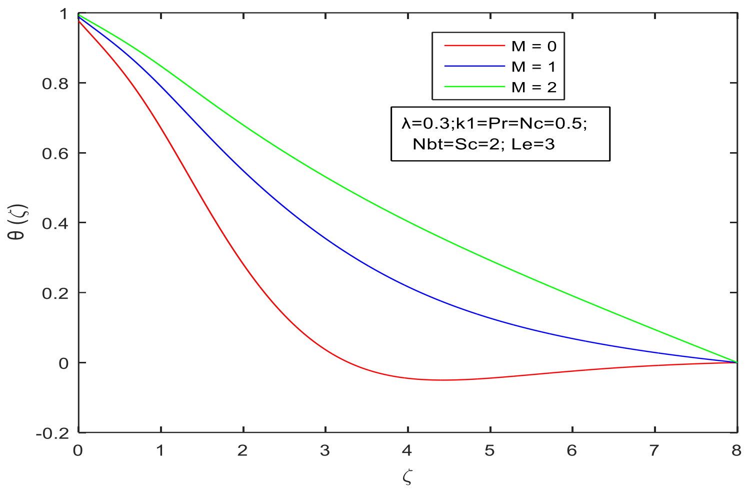

Fig. 4.11: Temperature with M.

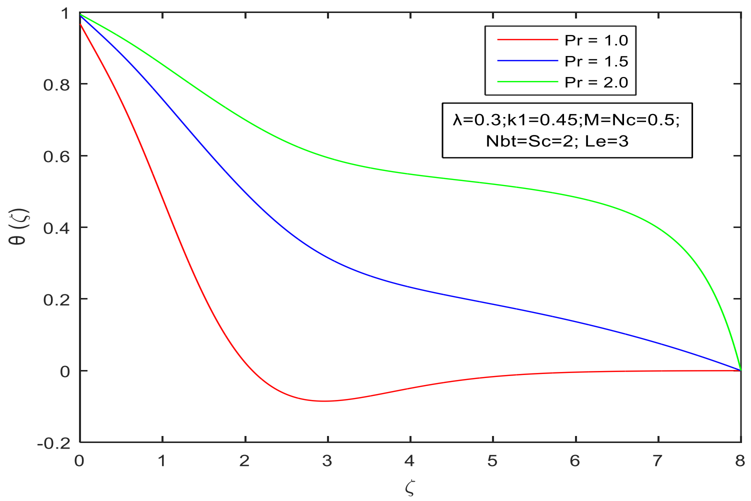

Fig. 4.12: Temperature with Pr.

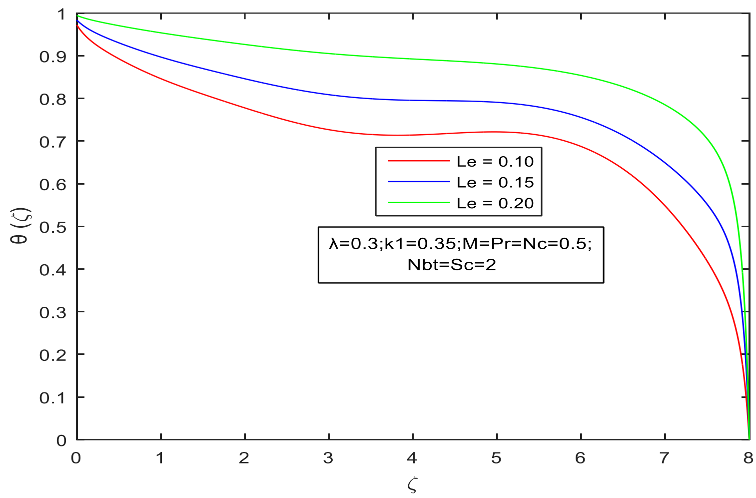

Fig. 4.13: Temperature with Le.

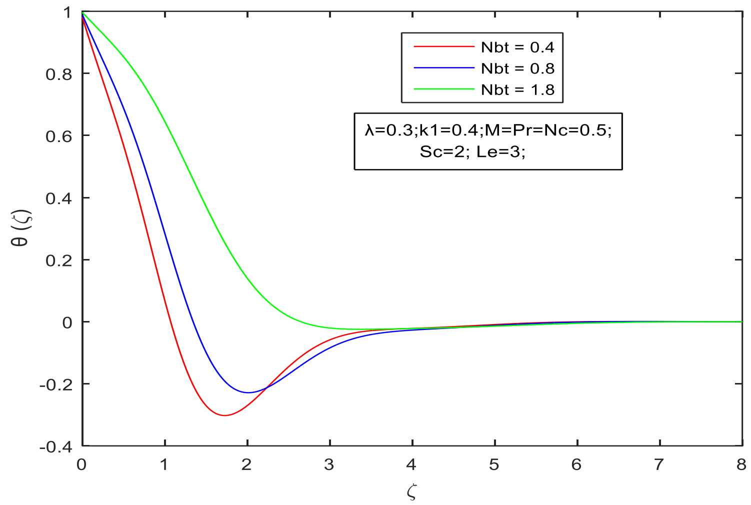

Fig. 4.14: Temperature with Nbt.

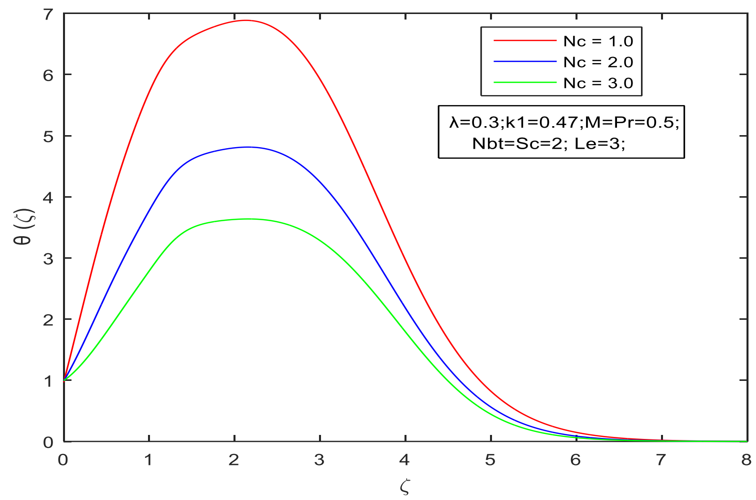

Fig. 4.15: Temperature with Nc

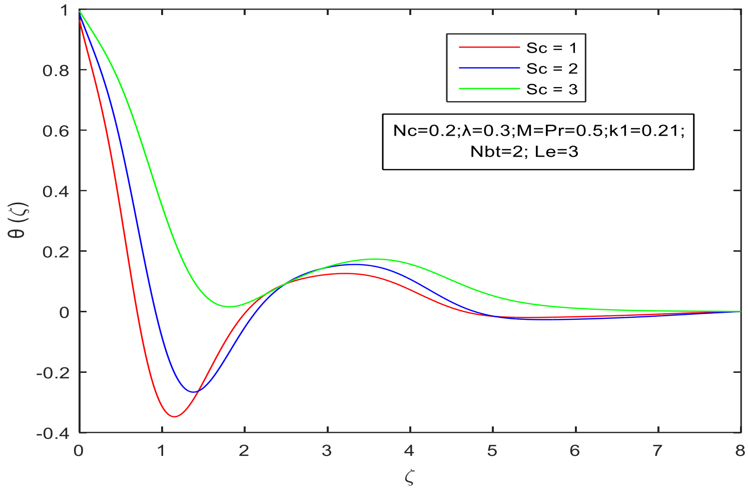

Fig. 4.16: Temperature with Sc.

Concentration Profile: The concentration distribution $\phi(\zeta)$ against ζ is illustrated in Figs. 4.17 – 4.24. It is observed that $\phi(\zeta)$ monotonically decreases within the nonlinear stretching sheet domain, satisfying the boundary conditions $\phi(\zeta) = 1$ at $\zeta = 0$ and asymptotically approaching $\phi(\zeta) = 0$ at $\zeta = 8$.

From Fig: 4.17: The concentration $\phi(\zeta)$ against ζ for assorted elastico-viscous parameters k_1. An augmentation of the elastico-viscous parameter $k_1(0.7 \rightarrow 0.9)$ intensifies the effective reaction rate, leading to a reduction in the concentration profile and a faster decay, because higher k_1 enhances species consumption, thereby lowering concentration levels and thinning the concentration boundary layer, which causes a more rapid decline away from the surface.

From Fig: 4.18: The variation of concentration $\phi(\zeta)$ against ζ for diverse values of the Williamson parameter λ reveals that elevating λ $(0.1 \rightarrow 0.5)$ markedly attenuates the concentration distribution and accelerates its asymptotic decay. This behavior is attributed to the intensification of non-Newtonian characteristics, whereby enhanced effective viscosity augments diffusive resistance,
consequently diminishing species transport and contracting the concentration boundary layer thickness.

From Fig: 4.19: The variation of concentration $\phi(\zeta)$ against ζ under varying magnetic parameter M reveals that augmenting M $(0 \rightarrow 2)$ significantly elevates the concentration distribution and attenuates its decay rate. This behavior is attributed to the intensified Lorentz force induced by the magnetic field, which suppresses fluid velocity, weakens convective mass transport, and consequently sustains higher species concentration within an expanded concentration boundary layer.

From Fig: 4.20: The variation of concentration $\phi(\zeta)$ against ζ is examined for varying Prandtl number Pr. An escalation in Pr $(1 \rightarrow 2)$ intensifies the concentration distribution and retards its attenuation rate. This behavior is attributed to the suppression of thermal diffusivity at elevated Pr, which diminishes the coupled thermo-diffusive interactions, thereby impeding mass transport. Consequently, the concentration boundary layer thickens, yielding a more progressive decay of $\phi(\zeta)$.

From Fig: 4.21: The concentration $\phi(\zeta)$ against ζ for different values of Lewis number Le. Higher Lewis number Le $(0.10 \rightarrow 0.20)$ reduces mass diffusivity, which weakens species diffusion, causing the concentration to decrease more rapidly and thereby inducing a diminished concentration boundary-layer thickness.

From Fig: 4.22: The concentration $\phi(\zeta)$ against ζ for different values of the diffusivity parameter Nbt. Higher diffusivity parameter Nbt $(0.4 \rightarrow 1.8)$ enhances nanoparticle diffusion, which increases species transport, causing the concentration to spread more and decay more gradually, resulting in a thicker concentration boundary layer.

From Fig: 4.23: The concentration $\phi(\zeta)$ against ζ for different values of heat capacity ratio parameter Nc. Higher heat capacity ratio Nc $(0 \rightarrow 4)$ increases energy absorption by the fluid, which reduces mass diffusion effects, causing the concentration to decrease and the boundary layer to become thinner.

From fig. 4.24: The concentration $\phi(\zeta)$ against ζ for different values of Schmidt number Sc. Higher Schmidt number Sc $(1 \rightarrow 3)$ reduces mass diffusivity, which weakens species diffusion, causing the concentration to decrease more rapidly and leading to a reduced concentration boundary-layer thickness.

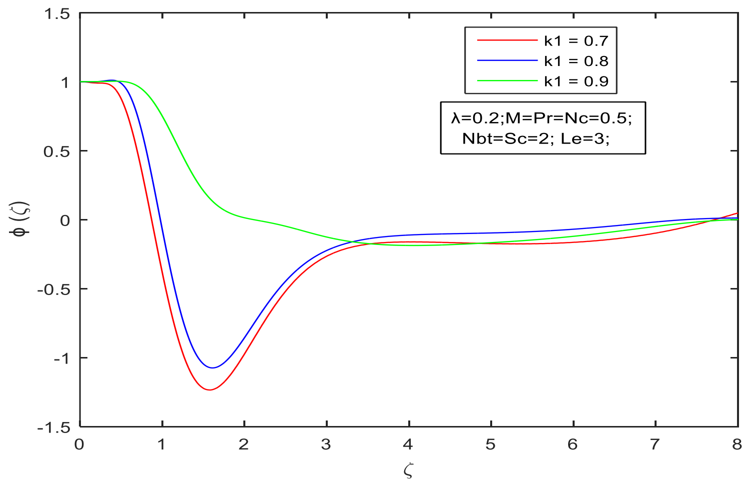

Fig. 4.17: Concentration with k1.

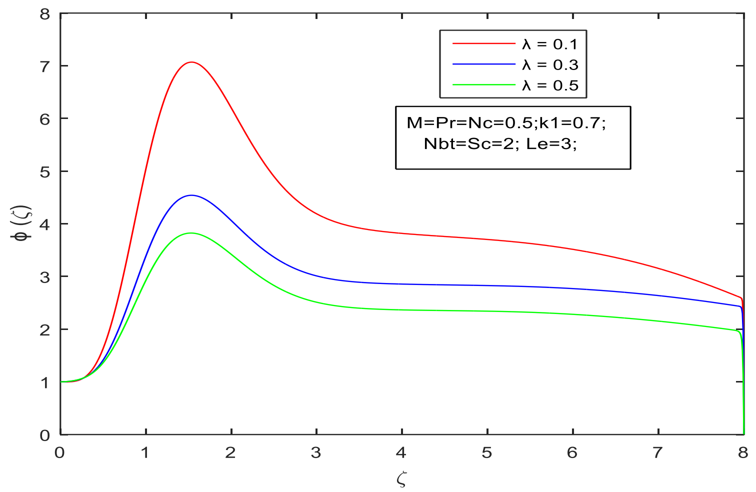

Fig. 4.18: Concentration with λ.

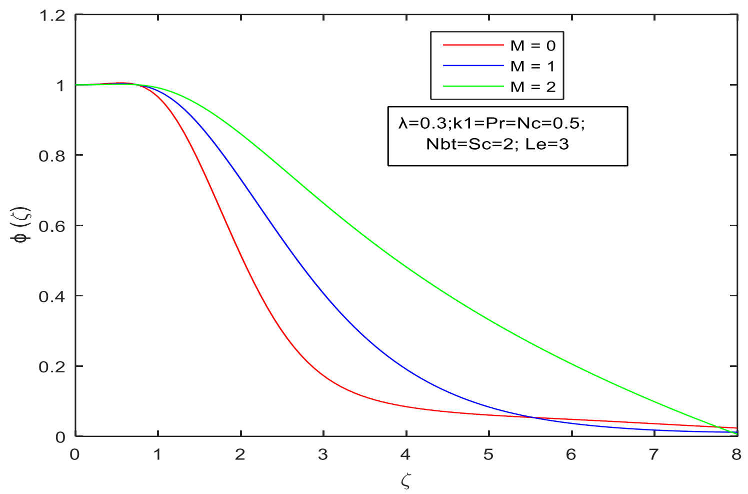

Fig. 4.19: Concentration with M.

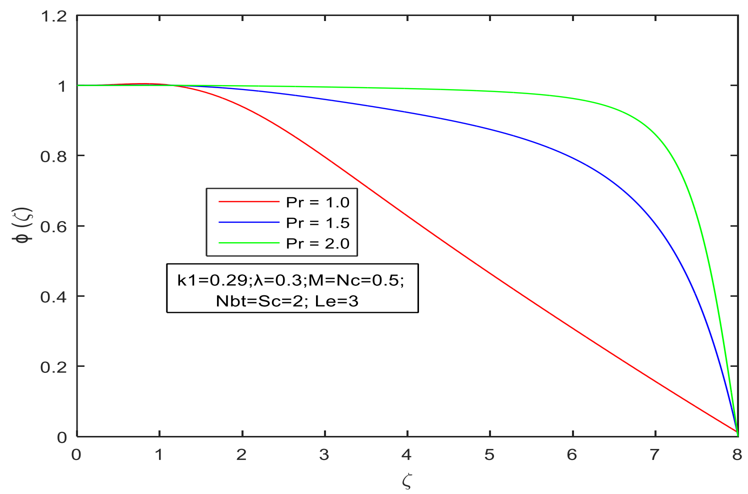

Fig. 4.20: Concentration with Pr.

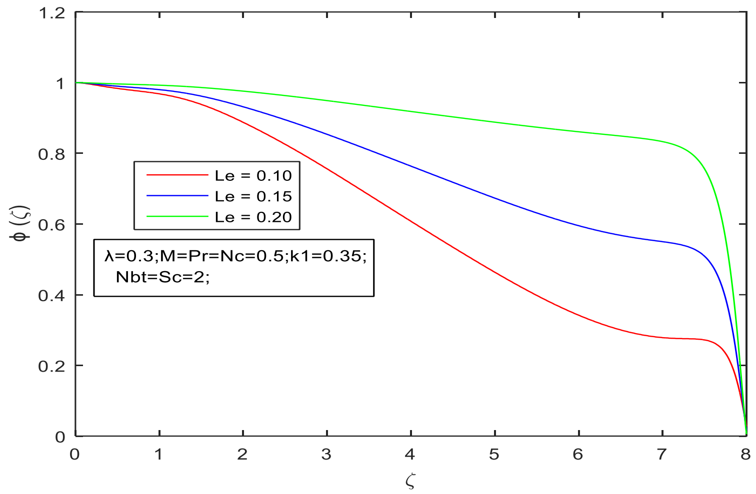

Fig. 4.21: Concentration with Le.

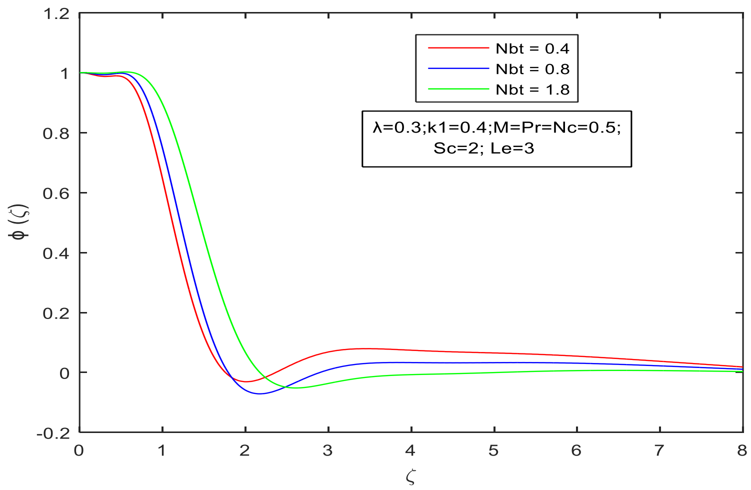

Fig. 4.22: Concentration with Nbt

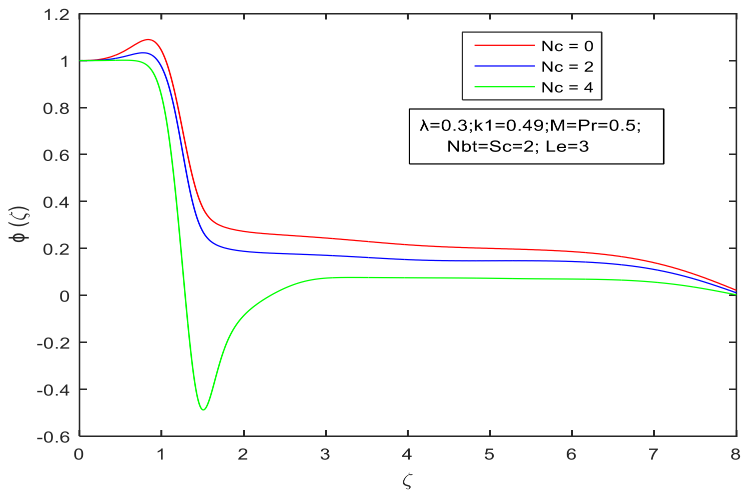

Fig. 4.23: Concentration with Nc.

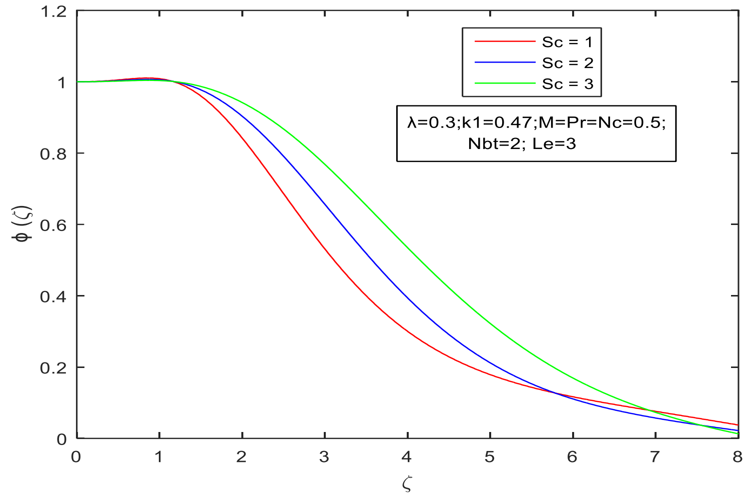

Fig. 4.24: Concentration with Sc.

Conclusion

This study models the magneto-hydrodynamic (MHD) boundary layer flow of an elastico-viscous Williamson nanofluid over a nonlinearly stretching sheet. Employing similarity transformations, the governing PDEs reduce to a coupled system of nonlinear ODEs. The investigation systematically probes the impact of the elastico-viscous parameter. k_1, Williamson parameter λ, magnetic parameter M, diffusivity ratio Nbt, Prandtl number Pr, Lewis number Le, Schmidt number Sc, and heat capacity ratio Nc on heat and mass transfer, with particular emphasis on isolating k_1, influence. Results underscore $k_1$as a pivotal factor governing boundary layer dynamics.
The key findings of this research are

- The velocity profile exhibits oscillatory and highly sensitive behavior due to the combined influence of elastico-viscous effects, magnetic damping, and nonlinear stretching. Parameters like elastico-viscous k_1 and Williamson λ enhance momentum transport and amplify oscillations, while magnetic parameter M, Lewis number Le, diffusivity Nbt, heat capacity ratio Nc, and Schmidt number Sc introduce resistive effects that suppress velocity and thin the boundary layer; meanwhile, a higher Prandtl number Pr strengthens momentum dominance and increases peak velocity. This behavior occurs due to the continuous competition between inertial forces (enhancing flow) and dissipative mechanisms (magnetic drag, viscous resistance, and diffusion), leading to alternating acceleration–deceleration within the boundary layer.

This study is highly relevant to magnetically controlled cooling systems in microelectronics (e.g., nanofluid cooling in electronic chips), where applying a magnetic field regulates fluid flow and heat transfer.
The imposed magnetic field induces a Lorentz force, modulating the fluid's dynamics, while nanoparticle diffusion and elastico-viscous effects adjust momentum and thermal transport—allowing precise tuning of cooling performance, stability, and efficiency in advanced thermal management systems.

- The temperature profile decays from the surface due to diffusion, but parameters such as elastico-viscous k_1, Williamson λ, magnetic M, Lewis number Le, and diffusivity Nbt enhance thermal energy, thereby increasing temperature and thickening the thermal boundary layer with slower decay; whereas higher Pr, Nc, and Sc suppress thermal diffusion or increase energy absorption, leading to lower temperature and faster decay. Physically, this behavior occurs due to the balance between heat generation/retention mechanisms (viscoelasticity, magnetic resistance, nanoparticle motion) and heat dissipation mechanisms (thermal and mass diffusivity).

A key application is in cooling of electronic devices using nanofluids under magnetic fields (MHD cooling systems)—where controlling parameters like M, Nbt, and Pr allow engineers to regulate heat removal efficiency; higher thermal retention (via k_1, λ, M) is useful for thermal stability, while higher Pr or Sc helps achieve rapid cooling, depending on design needs.

- The concentration field is strongly controlled by fluid elasticity, non-Newtonian behavior, magnetic effects, and diffusion parameters. Increasing k_1, λ, Le, Nc, and Sc suppresses concentration and accelerates decay due to enhanced resistance or reduced mass transport, yielding a contracted concentration boundary layer. In contrast, higher M, Pr, and Nbt elevate concentration and slow its decay by weakening convective or diffusive transport, thereby thickening the concentration boundary layer.

This behavior is highly relevant in magnetically controlled nanofluid coating processes (e.g., in microelectronics or biomedical surface engineering), where precise control of species concentration is required.
Because parameters like magnetic field M and nanoparticle diffusion Nbt regulate fluid motion and mass transport, engineers can tune concentration thickness and uniformity—either enhancing deposition (higher concentration, thicker layer) or promoting rapid consumption (lower concentration, thinner layer) depending on design needs.

Nomenclature

Symbol	Meaning	S.I. Unit
(u, v)	Velocity Component	(m/s)
U_w	Surface Velocity	(m/s)
T_w	Surface Temperature	(K)
C_w	Surface Concentration of nanoparticle	(mol/m^3)
B_0	Rate of Stretching Surface	-
$B*$	Magnetic parameter	-
T_∞	Ambient temperature	(K)
C_∞	Ambient Nanoparticle volumetric density	-
C	Concentration of nanoparticle	-
T	Fluid Temperature	(K)
D_T	Coefficient of Thermophoresis diffusion	$(m^{-2}s^{-1})$

D_B	Coefficient of Brownian diffusion	$(m^{-2}s^{-1})$
k_0	Elastoviscous Parameter	(Pa.S)
k_1	Transformed Elastico-viscous Parameter	(Pa.S)
M	Magnetic Parameter	-
Nbt	Diffusivity Parameter	-
Nc	Heat capacity ratio	-
Pr	Prandtl Number	-
Le	Lewis Number	-
Sc	Schmidt Number	-
f	Stream function	-
(x, y)	Cartesian coordinate	-

Greek Letter

Symbol	Meaning	S.I. Unit
υ	Kinematic viscosity	(m^2s^{-1})
μ	Dynamic viscosity	$(Kgm^{-1}s^{-1})$
ρ	Fluid density	(Kgm^{-3})
ζ	Similarity variable	-
α	Thermal diffusivity	(m^2s^{-1})
σ	Electrical Conductivity	(Sm^{-1})
θ	Dimensionless Temperature	-
$\emptyset$	Dimensionless Concentration	-
Γ	Positive time constant	-
λ	Williamson fluid	-
ρc	Heat capacity of the fluid	$(Jm^{-3}K^{-1})$
$\rho_p C_p$	Heat capacity of nanoparticle	$(Jm^{-3}K^{-1})$

Declarations

Funding

The authors declare that no specific funding was received for this work.

Conflicts of Interest

The author declares no conflicts of interest and confirms that this research was conducted independently without external funding or sponsorship.

Ethical Approval

This article does not contain any studies involving human participants or animals performed by the author.

Informed Consent

Not applicable.

Data availability

The data that support the findings of this study are available from the corresponding author upon reasonable request. However, most of the data generated or analyzed during this study are included in this article.

References

[1] Williamson, R. V. (1929). The flow of pseudo-plastic materials. *Industrial & Engineering Chemistry, 21*(11), 1108–1111. https://doi.org/10.1021/ie50239a035.

[2] Felder, E., & Levrau, C. (2011). Analysis of the lubrication by a pseudo-plastic fluid: Application to wire drawing. *Tribology International, 44*, 845–849. https://doi.org/10.1016/j.triboint.2011.02.009.

[3] Sohail Nadeem, S., & Noreen Sher Akbar, N. S. (2011). Numerical solutions of peristaltic flow of Williamson fluid with radially varying MHD in an endoscope. *International Journal for Numerical Methods in Fluids*, 66, 212–220. https://doi.org/10.1002/fld.2253.

[4] Berra, M., Carassiti, F., & Mangialardi, T. (2012). Effects of nanosilica addition on workability and compressive strength of Portland cement pastes. *Construction and Building Materials, 35*, 666–675. https://doi.org/10.1016/j.conbuildmat.2012.04.132.

[5] Syam Sundar, L., Venkata Ramana, E., Singh, M. K., & De Sousa, A. C. M. (2012). Viscosity of low volume concentrations of magnetic Fe_3O_4 nanoparticles dispersed in ethylene glycol and water mixture. *Chemical Physics Letters, 554*, 236–242. https://doi.org/10.1016/j.cplett.2012.10.042.

[6] Azmi, W. H., Sharma, K. V., Sarma, P. K., Mamat, R., Anuar, S., & Rao, V. (2013). Experimental determination of turbulent forced convection heat transfers and friction factor with SiO_2 nanofluid. *Experimental Thermal and Fluid Science, 51*, 103–111. https://doi.org/10.1016/j.expthermflusci.2013.07.006.

[7] Nadeem, S., Hussain, S. T., & Lee, C. (2013). Flow of a Williamson fluid over a stretching sheet. *Brazilian Journal of Chemical Engineering, 30*(3), 619–625. https://doi.org/10.1590/S0104-66322013000300019.

[8] Nadeem, S., & Hussain, S. T. (2014). Flow and heat transfer analysis of Williamson nanofluid. *Applied Nanoscience, 4*(8), 1005–1012. https://doi.org/10.1007/s13204-013-0282-1.

[9] Akbar, N. S., & Nadeem, S. (2014). Carreau fluid model for blood flow through a tapered artery with a stenosis. *Ain Shams Engineering Journal, 5*, 1307–1316. https://doi.org/10.1016/j.asej.2014.05.010.

[10] Azmi, W. H., Sharma, K. V., Sarma, P. K., Mamat, R., & Anuar, S. (2014). Comparison of convective heat transfer coefficient and friction factor of TiO_2 nanofluid flow in a tube with twisted tape inserts. *International Journal of Thermal Sciences, 81*, 84–93. https://doi.org/10.1016/j.ijthermalsci.2014.03.002.

[11] Sreedevi, P., Reddy, P. S., & Chamkha, A. J. (2017). Heat and mass transfer analysis of nanofluid over linear and non-linear stretching surfaces with thermal radiation and chemical reaction. *Powder Technology, 315*, 194–204. https://doi.org/10.1016/j.powtec.2017.03.059.

[12] Jahan, S., Sakidin, H., Nazar, R., & Pop, I. (2017). Flow and heat transfer past a permeable nonlinearly stretching/shrinking sheet in a nanofluid: A revised model with stability analysis. *Journal of Molecular Liquids, 233*, 211–221. https://doi.org/10.1016/j.molliq.2017.03.013.

[13] Khan, U., Ahmad, S., Hayyat, A., Khan, I., Nisar, K. S., & Baleanu, D. (2020). On the Cattaneo–Christov heat flux model and OHAM analysis for three different types of nanofluids. *Applied Sciences, 10*, 886. https://doi.org/10.3390/app10030886.

[14] Hussain, Z., Hayat, T., Alsaedi, A., & Ullah, I. (2021). On MHD convective flow of Williamson fluid with homogeneous–heterogeneous reactions: A comparative study of sheet and cylinder. *International Communications in Heat and Mass Transfer, 120*, 105060. https://doi.org/10.1016/j.icheatmasstransfer.2020.105060.

[15] Ahmed, K., McCash, L. B., Akbar, T., & Nadeem, S. (2022). Effective similarity variables for the computations of MHD flow of Williamson nanofluid over a non-linear stretching surface. *Processes, 10*(6), 1119. https://doi.org/10.3390/pr10061119.

[16] Muzara, H., & Shateyi, S. (2023). Magneto-hydrodynamics Williamson Nanofluid Flow over an Exponentially Stretching Surface with a Chemical Reaction and Thermal Radiation. Mathematics, 11 (12), 2740. https://doi.org/10.3390/math11122740.

[17] Rashad, A. M., Nafe, M. A., & Eisa, D. A. (2023). Heat variation on MHD Williamson hybrid nanofluid flow with convective boundary condition and Ohmic heating in a porous material. *Scientific Reports, 13*, 6071. https://doi.org/10.1038/s41598-023-33043-z.

[18] Khan, K. A., Javed, M. F., Ullah, M. A., & Riaz, M. B. (2023). *Heat and mass transport analysis for Williamson MHD nanofluid flow over a stretched sheet*. Results in Physics, *53*, 106873. https://doi.org/10.1016/j.rinp.2023.106873.

[19] Madan Kumar, R., Srinivasa Raju, R., Mebarek-Oudina, F., Anil Kumar, M., & Narla, V. K. (2024). Cross-diffusion effects on an MHD Williamson nanofluid flow past a nonlinear stretching sheet immersed in a permeable medium. *Frontiers in Heat and Mass Transfer, 22*(1), 15–34. https://doi.org/10.32604/fhmt.2024.048045.

[20] Sakkaravarthi, K., & Bala Anki Reddy, P. (2024). Entropy generation on MHD flow of Williamson hybrid nanofluid over a permeable curved stretching/shrinking sheet with various radiations. *Numerical Heat Transfer, Part B: Fundamentals, 85*(3), 231–257. https://doi.org/10.1080/10407790.2023.2231633.

[21] Ramadevu, S., Vijaya Kumar, P., Ibrahim, S. M., & Jyothsna, K. (2025). Investigation of heat and mass transfer in magnetohydrodynamic Williamson nanofluid flow over a nonlinear stretching surface with viscous dissipation and radiation effects: A numerical approach. *Radiation Effects and Defects in Solids, 180*(9–10), 1331–1352. https://doi.org/10.1080/10420150.2025.2467348.

[22] Gizachew, B., Dessie, H., Haile, E., & Wallelign, T. (2025). Investigation of time-dependent MHD flow characteristics of Williamson nanofluid across a heated, permeable and inclined stretching sheet within a porous medium. *Physics Open, 25*, 100349. https://doi.org/10.1016/j.physo.2025.100349.

[23] Sankari, S., Rao, M. E., Elsiddieg, A. M., Khan, W., Makinde, O. D., Saidani, T., Kraiem, N., & Garalleh, A. L. H. (2025). Analytical solution of MHD bioconvection Williamson nanofluid flow over an exponentially stretching sheet with the impact of viscous dissipation and gyrotactic microorganism. *PLOS ONE, 20*(3), e0306358. https://doi.org/10.1371/journal.pone.0306358.